Light in the Darkening on Naica Gypsum Crystal

I. Castillo-Sandoval, L. E. Fuentes-Cobas, M.E. Fuentes-Montero, H. E. Esparza-Ponce, J. Carreno-Márquez, M. Reyes-Cortes, M. E. Montero-Cabrera

Naica mine is located in a semi-desertic region at the central-south of Chihuahua State. The Cave of Swords was discovered in 1910 and the Cave of Crystals 90 years later at Naica mines. It is expected that during the last century the human presence has changed the microclimatic conditions inside the cave, resulting in the deterioration of the crystals and the deposition of impurities on gypsum surfaces. As a contribution to the clarification of the mentioned issues, the present work refers to the use of synchrotron radiation for the identification of phases on these surfaces. All the experiments were performed at the Stanford Synchrotron Radiation Lightsource. Grazing incidence X-ray diffraction (GIXRD) and radiography-aided X-ray diffraction (RAXRD) experiments were performed at beamline 11-3. X-Ray micro-fluorescence (μ-SXRF) and micro-X-ray absorption (μ-XANES) were measured at beamline 2-3. Representative results obtained may be summarized as follows: a) Gypsum, galena, sphalerite, hematite and cuprite at the surface of the gypsum crystals were determined. b) The samples micro-structure is affected by impurities. c) The elemental distributions and correlations (0.6-0.9) of Cu, K, Fe, Mn, Pb, Zn, Ca and S were identified by μ-SXRF. The correlations among elemental contents confirmed the phase identification, with the exception of manganese and potassium due to the amorphous nature of some impurity compounds in these samples. The compounds hematite (Fe2O3), β-MnO2, Mn2O3, MnO and/or MnCO3, PbS, PbCO3 and/or PbSO4, ZnO4, ZnS and/or smithsonite (ZnCO3), CuS + Cu

Oxide were identified by XANES. Plausibly, these latter compounds do not form crystalline phases.

Naica mine is located in a semi-desertic region at the central-south of Chihuahua State; its galleries have been worldwide famous due to the dimension and purity of their gypsum crystals [1-6]. The most famous caves are: “Cueva de las Espadas” (Cave of Swords) and “Cueva de los Cristales Gigantes” (Giant Crystals Cave). These spectacular giant crystals attracted immediately the attention of the scientists, who described several cave features [1-15]. In the last decade there have been studies focused on establishing theories of nucleation and crystal growth in the Cueva de los Cristales Gigantes [3, 4, 8-10]. The calculated temperature at which the crystals have grown must be close to the transition temperature between gypsum and anhydrite [11]. The calculated growth rate was 1.4 ± 0.2

× 10-5 nm/s [8]. The calculated age is between tens and hundreds thousands years [5].

References [6, 13] suggest possible antropogenic and natural alterations in the caves. Authors of [6, 12] suggest that at the “Ojo de la Reina” (Queen’s Eye cave) the incongruent dissolution of gypsum crystals would form calcite deposition on their surface. References [14, 15] describe that at the Cave of Swords, a unique speleothem which consists on a high-purity selenite core covered by successive deposits of calcite, gypsum and aragonite. There are other studies that mention the different colors that can be present in gypsum, for instance, yellow, orange and red are associated to iron, green to chromium, brown to the presents of clays and black to manganese [16]. Some destructive analytical techniques [4] and [7] have

identified other impurities. However, there are no studies on changes in the color of the gypsum crystals surface, which appear to be caused by environmental influences, being such an alteration a possible evidence of corrosion.

The aim of this work is to characterize the impurities on the surface of gypsum crystals. The study focuses on the Cave of Swords and the Giant Crystals Cave. These caves have been in contact with humans in the last 100 and 15 years respectively. Generally the impurities are deposited on the (010) face, making it difficult to perform analysis without destroying or altering the sample. Due to their superficial nature, determining the phases by traditional methods is difficult. The use of non-destructive techniques is the key to unlock the secrets that still hold the gypsum single crystals at Naica. Therefore, synchrotron radiation (SR) provides a great tool for analysis and determination of impurities on gypsum single crystals surfaces.

Materials and Methods

Figure 1 shows representative images of original crystals from the Cave of Giant Crystals and the Cave of Swords. The outer surface of the crystal from the later cave is very dark as a result of the presence of impurities, and the thickness of the surface layer is estimated in the order of 1 cm. The Cave of Giant Crystals is recognized by the clearness of the gypsum crystals, i.e., by the low presence of impurities on its surface.

Figure 1. At the left a crystal of gypsum which is displayed at the Harvard Museum of Natural History is presented. The gypsum crystal has a cut on the surface layer. The scale bar is 10 cm long. At the right, a general view of the Giant Crystals cave, where persons in the background can be seen inside the oval, is shown

Figure 2. Samples of Naica gypsum Crystals. From left to right are displayed: the “Harvard” sample, the Cave of Swords main sample, and some parts of the Giant Crystal Cave sample studied in the present work.

In the present work, samples collected from the Cave of Swords and from the entrance of the Giant Crystals cave, which was given by the Natural History Museum of Harvard University and private collectors, were examined. Specifically, twelve samples for mineralogical and geochemical analyses from the Cave of Swords and 10 samples from the Giant Crystals Cave were investigated by synchrotron radiation. More than 80 2D XRD patterns, 100 distribution maps by XRF, and 30 XANES spectra were performed. Obtained gypsum crystal samples show a wide diversity of appearances and dimensions. Only those samples presenting surface

impurities and solid inclusions within the gypsum crystals were selected for the analysis. Crystal samples were cut in slices by the exfoliation plane (010) of gypsum. Figure 2 shows examples of the samples under study.

Synchrotron light source techniques

Grazing incidence X-Ray Diffraction (GIXRD) at a synchrotron facility was performed by a two-dimensional (2-D) scattering measurement system [17-19]. Scattered intensity distribution was collected by means of a twodimensional charge-coupled device (CCD) detector. Irradiation was usually done with incident angles below and above the critical angle for total reflection, $\phi_{crit} = 0.14^{o}$. Larger incident angles were used to explore the sample volume. In the same station, Radiography Aided X-Ray Diffraction (RAXRD) experiments could be performed as well. This is done by scanning a sample crosswise and recording transmitted photons. Measurement time per scattering pattern varied from a few seconds to several minutes, which is a significantly smaller time than what is customary in conventional-source diffractometry. The interpretation of collected 2-D CCD patterns, leading to maps of scattered intensity as a function of reciprocal space coordinates (for GIXRD) or sample density (for RAXRD), was performed with the aid of programs SPEC [20] and Wxdiff [21].

GIXRD (reflection) and RAXRD (transmission) measurements were performed at the beamline 11-3 of the Stanford Synchrotron Radiation Lightsource (SSRL) using a wavelength (λ) of 0.09744 nm. For GIXRD the incidences angles were 0.1, 0.2, 0.3, 0.5, 1, 2 and 3°; the last angle produces a penetration depth in

gypsum of 20 μm; the spot size was 0.15 × 0.15 mm^2. The sample to detector distance was 150 mm; the 2D-detector used was model MAR345 with screen pixel dimensions of 150 ξ 150 μm^2. The 2D patterns were recorded with in-house software tools [21]. The modulus of the scattering vector s ($|s| = 4\pi \cdot \sin\theta/\lambda$ where θ is the Bragg angle) was calibrated using several intense reflections of LaB_6 powder. The experimental Debye rings were processed with the FIT2D software [22], followed by its simulation with the software [23] and “ANAELU” [24].

The synchrotron radiation micro X-ray fluorescence (SR-μ-XRF) imaging technique at SSRL provides great analytical capabilities due to its intense, collimated, polarized, and tunable X-ray beams. It is the best way to analyze the surface impurities on samples [2527]. In the present study, elemental maps were collected on thin sections at SSRL on beamline 2-3, using a Si (111) monochromator crystal, a 2 x 2 μm^2 incident beam cross-section and a single element vortex detector; where measured fluorescence related to concentrations of excited elements. Images were collected with a pixel step size of 2 μm, a 250 ms dwell time and an excitation energy of 13100 eV corresponding to Pb LIII edge. The penetration depth for μ-XRF experiments is 340 μm maximum. After XRF maps were collected, the analysis was applied to pixel images to locate regions of interest and unique chemical/spectral differences using SMAK (version 1.01) [28]. Based on the results of this analysis, representative pixel regions were selected for micro-focused X-ray absorption near edge structure (μ-XANES) analysis using a 2 μm^2 spot size. By means of X-ray absorption near edge structure (XANES) it is possible to characterize the oxidation state, electronic configuration and the local symmetry

nearby the absorbing atom [29].

μ-XANES data reduction was performed by averaging replicate scans using the software “SIXPack” (version 1.1) [30] after energy calibration. The X-ray energy calibration was performed by defining the maximum of metal foil spectra as: Pb LIII-edge =13035 eV, Zn K-edge = 9659 eV, Cu K edge= 8979 eV, Fe K-edge= 7112 eV and Mn K-edge =6539 eV [31]. After data processing steps, including magnification correction and image alignment, XANES spectra for each single pixel were generated by plotting the intensity values of the corresponding pixel through the stack of images vs. energy. The edge jump height of the spectrum in each pixel was plotted as a transparency map indicating the concentration of Pb, Mn, Fe, Cu and Zn ions.

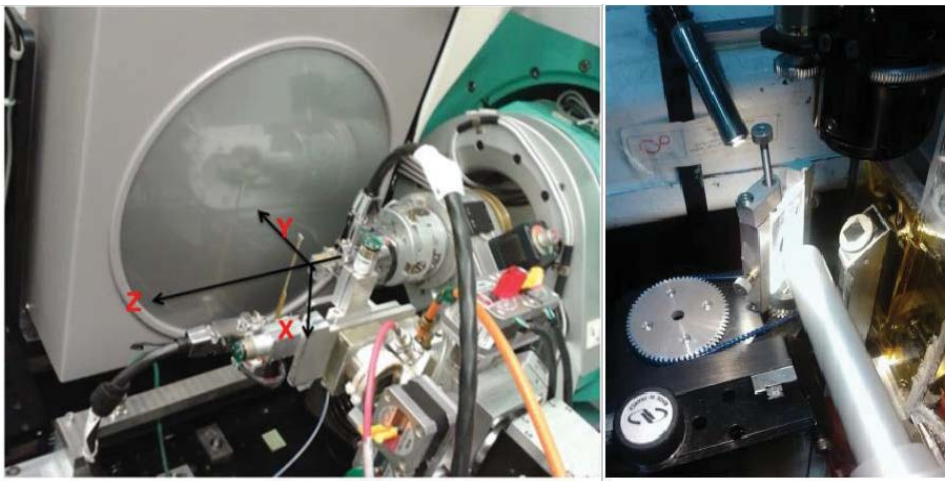

Figure 3. Synchrotron light techniques configurations at BL 11-3 and 2-3 at SSRL. Left: 2D-detector MAR345 is shown in front of the sample holder. The X-ray beam comes from the right-bottom corner of the picture and is recorded by transmission at the MAR345. The X, Y, Z system of coordinates of the movements performed in the RAXRD experiment is displayed. The Y-axis corresponds to the incident beam path. When the GIRXD experiment is performed, the sample is placed horizontally on the sample holder and the angle of incidence is set by the angular movement of the sample holder. Right: the layout of BL 2-3, where SR-μ-XRF is performed, is presented. The picture shows the high performance silicon drift detector Vortex at front, while the Xray beam comes from the right.

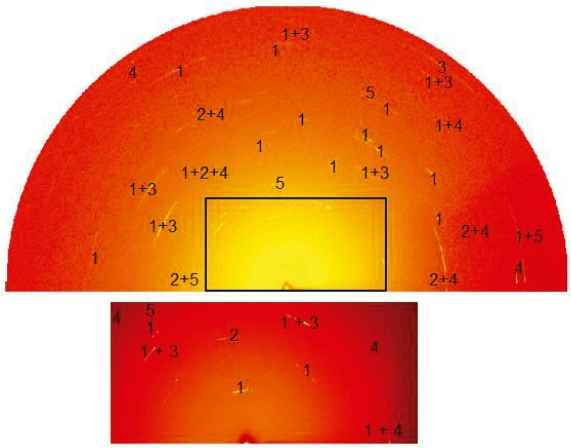

Phases (#)	Miller Indexes
Gypsum (1)	020, 040,-211,060,-202,071,-233,262,-332,-341,310, 202,-363,-341,310,-163, 202,-363,341,2100,-451
Galena (2)	,
Sphalerite (3)	111, 022,024,116,004
Hematite (4)	002, 022,113,133
Cuprite (5)	110,113,222,124,0110, 134
	111,002,123,113

Figure 4. 2D-XRD Pattern and interpretation of the GIXRD from the sample “Gigantes 3” from the Giant Crystal Cave. The identification numbers on the spots and/or lines are linked with the corresponding phases in the table.

Figure 4 shows a pattern of the GIXRD of the sample “Gigantes 3”, for an incidence angle of 0.5°. The identification of impurity phases in the Giant Crystals Cave gave as result: hematite (Fe2O3), cuprite (Cu2O), sphalerite (ZnS) and galena (PbS). All the mentioned impurities were also found in the crystals from the Cave of sSwords, where chalcopyrite (CuFeS2) and alabandite (MnS) were as well identified. Also, all these mentioned phases are known to be phases that crystallyze at temperatures higher than 300 °C, mostly above 400 °C.

Radiography aided X-Ray Diffraction.

Figure 5 shows the patterns obtained by RAXRD. The radiography shows how the sample has absorbed the Xrays by the intensities of the transmitted X-rays, registered in the MARS345 detector. Impurities in the sample increase from left to right, as was observed by direct inspection. The successive changes in the shape of diffraction spots at 2D-XRD patterns, from left to right in the sample, suggest the increasing alteration of the single crystal, which acquires a mosaic microstructure.

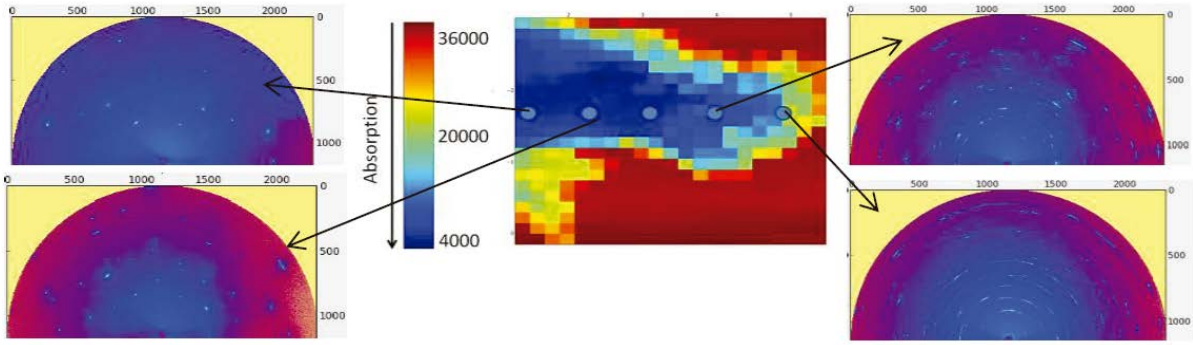

Figure 5. 2D-XRD patterns of RAXRD experiment, performed to one section of the “Harvard” sample. At the center of this figure, the image of transmitted X-rays recorded pattern is displayed. The spots represent the coordinates of points where 2DXRD was performed. At the left, the patterns show increasing sizes of the diffracted spots. At the right, at the points closer to the sample impurities, it can be seen that the spots became lines.

X-ray fluorescence and X-ray absorption near edge structure.

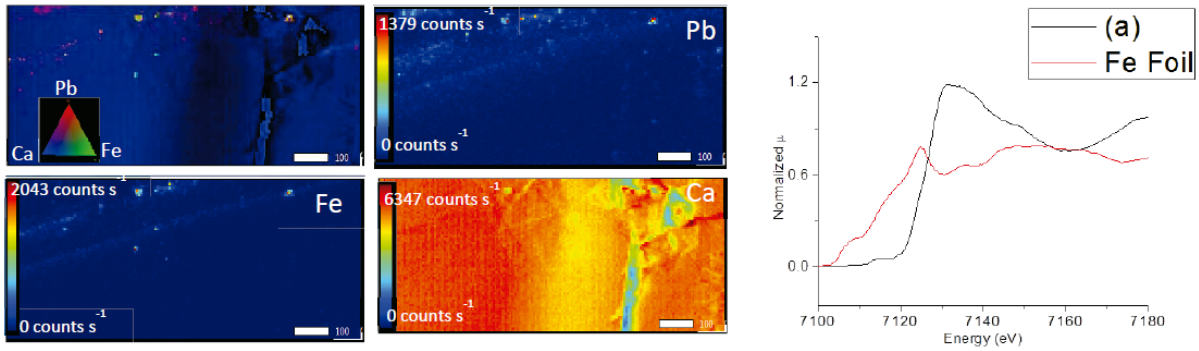

Figure 6. X-ray fluorescence map (left) and XANES (right) of sample “SWES021” from the Cave of Swords. Scale Bar 100 μm.

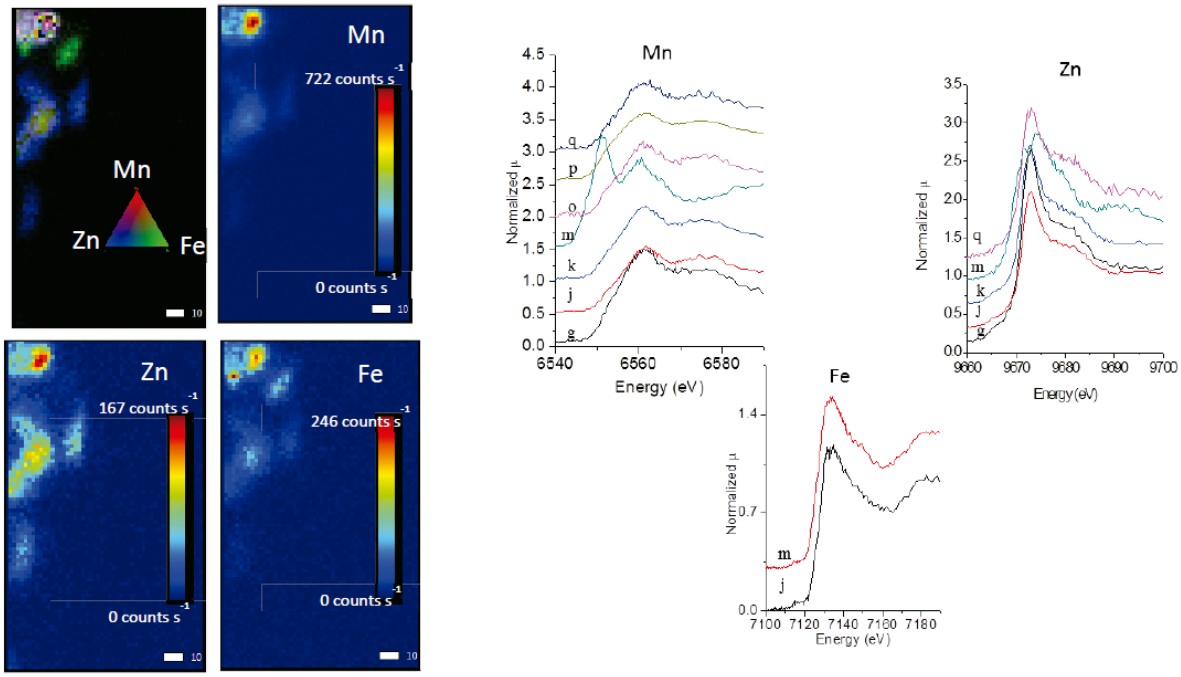

Figure 7. X-ray fluorescence map (left) and XANES (right) of sample “Giants 3” Region 4. The main peaks of Mn were assigned respectively to 6550 eV, 6560 eV, and 6575 eV. The energies 9658 eV, 9661 eV, and 9666 eV are the three characteristic peaks for Zn in minerals. Fe K-edge XANES shows a pre peak at 7120eV. The spectra were shifted upward and downward for clarity. Scale Bar corresponds to 10μm.

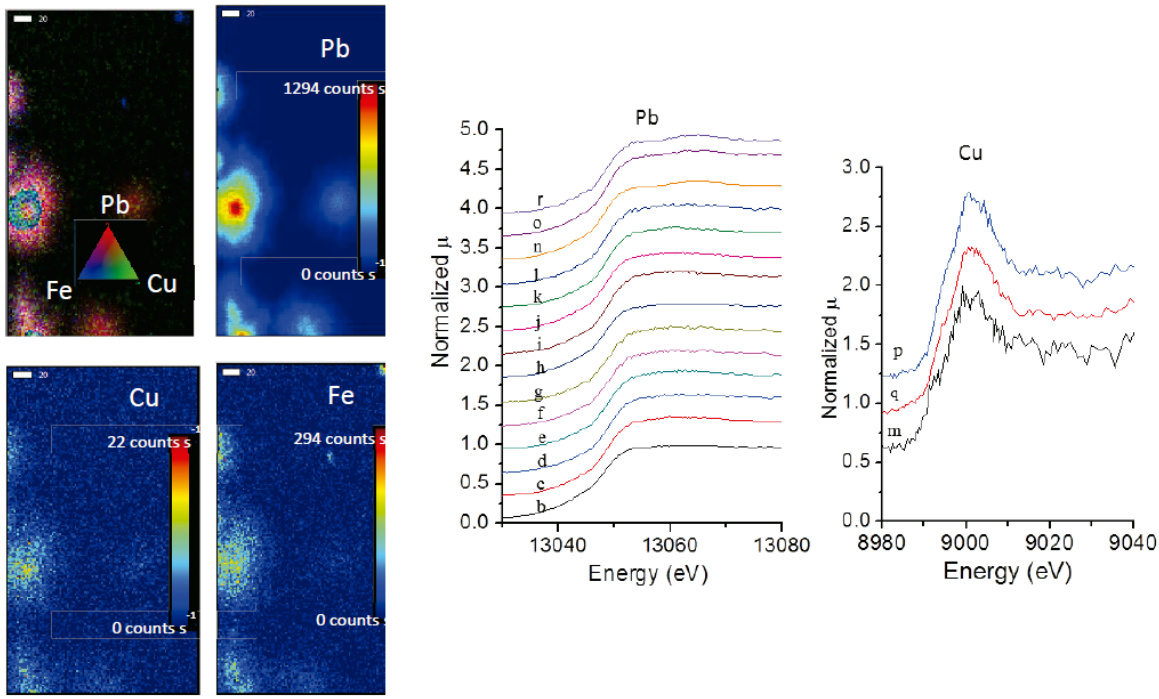

Figure 8. At left hand are presented the X-ray fluorescence mappings of sample "R290 3" Region 1, the scale bars are of 20μm. At center are shown the Pb K-edge XANES spectra and at right hand, the Cu K-edge XANES spectra collected in fluorescence yield mode for different sample regions, presented in Table 1.

Figures 6, 7 and 8 show the elemental distribution maps of sample study areas and spectra obtained by the application of SR μ-XRF and μ-XANES to the samples. The elemental distributions, with correlation values between 0.6 and 0.9 for the map concentrations of Cu, K, Fe, Mn, Pb, Zn, Ca and S, and the comparison of the shape of spectra with those of model compounds, led to the interpretation presented in Table 1.

The analysis of the shape of the μXANES spectra at the Fe K-edge suggests that hematite is present in all studied samples. Figures 6 and 7 present Fe μXANES spectra, having a pre-peak at around 7120 eV, attributed to 1s-3d photoelectron transition [32], a dipole forbidden process [33]. In the same figures, the shoulder at

7150 eV cannot be attributed to a particular characteristic of Fe^{2+}, because XANES signals in this region correspond to oscillations in the coordination state of Fe atoms [34]. The interpretation of these spectra corroborates the results of GIXRD in this paper and the identification reported by [7]. The shape of the μXANES spectra for Mn K-edge allowed identifying the amorphous Mn-oxides, by comparison with the model compounds shown in [35]. From Figure 8, by comparison of the Pb-LIII edge μXANES spectra of the samples with those of models compounds reported in [36], it is suggested that the impurities on crystal samples might include chemical forms of PbS, PbO, $PbSO_4$ and/or $PbCO_3$.The presence of these compounds among the impurities suggest changes in the pH of the aquifer in Naica [37]. Also in Figure 8, the shape of the Cu K-edge μXANES spectra suggests the presence of CuS and/or Cu oxide. These compounds suggest the oxidation of $CuFeS_2$ at the samples surface [40].

We did not find incongruent dissolution phases i.e. CaCO3 as new phase by the interaction of CaSO4·H2O with CO2 suggested by [6] and [12] related to any of the samples

Samples	Mn	Fe	Cu	Zn	Pb
(a)SWES021		Fe_2O_3			
(b)Gigants1_reg1					PbS
(c)Gigants2_reg1					$PbSO_4$
(d)Gigants2_reg2.1					$PbSO_4$
(e)Gigants2_reg3					$PbSO_4$
(f)Gigants2_reg4					$PbSO_4$
(g)Gigants3_reg1	β-MnO_2[35]			$ZnSO_4$[38]	PbS
(h)Gigants3_reg2					PbS
(i)Gigants3_reg3					PbS
(j)Gigants3_reg4	β-MnO_2[35]	Fe_2O_3		$ZnSO_4$[38]	PbS
(k)Gigants3_reg5	β-MnO2[35]			$ZnSO_4$[38]	PbS
(l)Gigants4_reg4					PbS
(m)R290_1_reg1	$MnCO_3$[35]	Fe_2O_3	CuS	$ZnCO_3$[39]	
(n)R290_2_reg1					$PbSO_4$+PbO
(o)R290_3_reg1	Mn_2O_3[35]				$PbCO_3$
(p)R290_3_reg2	β-MnO_2[35]		CuO		
(q)R290_3_reg3	MnO[35]		CuO	ZnS[38]	
(r)R290_4_reg1					PbO

TABLE 1. Interpretation of μXANES spectra. The labels in figures 7 and 8 correspond to the identification of samples shown in parenthesis.

Conclusions

The use of non-destructive techniques as the key to unlock the secrets of gypsum single crystals at Naica still holds. GIXRD is a great tool for determining impurities in gypsum single crystals surfaces that cannot be identified by traditional methods. In this study, RAXRD was useful in revealing the crystal microstructure. The elemental analyses by μ-XRF were helpful at identifying the distribution of elements and compounds. The μ-XANES method was a powerful tool when identifying amorphous compounds and at estimating the contribution of anthropogenic materials to the mineral phase. In general, the hematite has appeared as a surface impurity in all studied samples. Several other phases non-detectable by conventional techniques were identified and characterized by synchrotron radiation methods.

Acknowledgments

The support given by Consejo Nacional de Ciencia y Tecnología Project No. 183706 is acknowledged. GIXRD, TX, XRF and XAS spectra were measured (as part of Proposal No. 3939) at the Stanford Synchrotron Radiation Lightsource (SSRL), a Directorate of SLAC National Accelerator Laboratory and an Office of Science User Facility operated for the U.S. Department of Energy Office of Science by Stanford University. Authors want to thank the Harvard Museum of Natural History for the support given for providing the sample. Also the authors give thanks to Juan Manuel Garcia-Ruiz, for his valuable suggestions.

References

1. W.F. Foshag, American Mineralogist, 12, 252-256(1927)
2. L. M. Alva-Valdivia *et al.,* Earth Planets Space, 55, 19–31 (2003)
3. B. R. Marín Herrera *et al.,* Boletín de Mineralogía, 17,139 – 148(2006)
4. J.M. García-Ruiz *et al.,* Geology, 35, 327-330 (2007).
5. L. Sanna *et al*., International Journal of Speleology, 39(1), 35-46. Bologna (Italy). (2010).
6. P .Forti, and L. Sanna.Episodes, 33 (1), 23–32 (2010).
7. P. S. Garofalo *et al.,* Earth and Planetary Science Letters 289 560-569 (2010).
8. A.E. Van Driessche *et al.,* Proc Natl Acad Sci U S A 108, 15721. (2011).
9. A.E Van Driessche *et al.,* Science, 336 69-72 (2012).
10. Y. Kruger *et al.,* Geology, 41 119-122 (2012).
11. J.M. García-Ruiz *et al.,* Chem. Soc. Rev., 2014,43, (2013)
12. T.Bernabei *et al.,* International Journal of Speleology, 36 (1), 23-30 Bologna (Italy). (2007)
13. G. Badino *et al.,* International Journal of Speleology, 40 , 125-131 (2011)
14. F. Gazquez *et al.,* International Journal of Speleology, 41(2), 211-220.(2012)
15. F. Gazquez *et al.,* Quaternary Research 80, 510–521(2013)

16. Sharpe, R., & Cork, G. *Industrial Minerals & Rocks: Commodities, Markets, and Uses*(2006)
17. J Als-Nielsen *et al.,* Phys Rep 246, 251 (1994)
18. I Kuzmenko *et al.,* Chem Rev 101:1659 (2001)
19. L. Fuentes: "Synchrotron Radiation Diffraction and Scattering in Ferroelectrics". Chapter 6, Multifunctional polycrystalline ferroelectric materials. Editors: L. Pardo y J. Ricote, Springer-Verlag, Dordrecht (2011)
20. SPEC software: http://www.certif.com/index.html
21. S.C. Mannsfeld, WxDiff version 1.11 (http://code.google.com/p/wxdiff) SSRL, (2009)
22. A P. Hammersley, FIT2D V12. 012 Reference Manual V6. 0,(2004.)
23. L. Fuentes-Montero *et al.,* Journal of Applied Crystallography, 44, 241-246. (2011)
24. ANAELU software: http://cimav.edu.mx/investigacion/software/anaelu (2010)
25. U. Bergmann *et al.,* Proc Natl Acad Sci U S A, 107 9060-5 (2010)
26. U.Bergmann *et al.,* Phys World, 20,39-42 (2007)
27. B.F. Popescu *et al.,* Phys Med Biol, 54, 651-663. (2009)
28. S. M. Webb, AIP Conference Proceedings, 1365, 196-199(2011)
29. NEXAFS Spectroscopy, J. Stöhr/Springer-Verlag, Berlin, (1992)
30. S. M. Webb, SixPACK software, Physica Scripta T115, 1011-1014. (2005)
31. W.T. Elam *et al.,*Radiation Physics and Chemestry 63, 121-128 (2002)
32. H.Y. Chen *et al.,* J. Mol. Catal. A, 162, 159 (2000).
33. N. Kaurav *et al.,* Applied Physics Letters 94, 192507 (2009)
34. M. S. Batista *et al.,* Braz. J. Chem. Eng. 22 no.3 São Paulo (2005)
35. S.J.A. Figueroa *et al.* Catalysis Today 107–108 849–855(2005)
36. K. Funasaka *et al.* Science of the Total Enviroment 403 230– 234 (2008)
37. K. A.Hudson-Edwards *et al.,* Environmental Science & Technology 30, 72-80.(1996)
38. R.A.Root *et al.,* Applied Geochemistry, doi: http://dx.doi.org/10.1016/j.apgeochem.2015.01.005 (2015)
39. G. A. Waychunas *et al.,* Geochimica et Cosmochimica Acta, 67, 1031–1043, (2003)

40. R.A.D. Pattrick Int. J. Miner. Process. 55 247–265. (1999)